Supporting Information

Integrating of Sequential Chemical State Transformations in Bifunctional Copper-based Metal-Organic Frameworks for Self-Powered Photocatalytic Reaction Systems

Yuanmeng Tao[a], Chao Huang [a,*], Jiaxing Cui[a], Dandan Wang[a], Qi Qin[a], Jichao Wang[b,*], Zhichao Shao[a,*]

[a]School of Materials Electronics and Energy Storage and Center for Advanced Materials Research, Zhongyuan University of Technology, Zhengzhou, Henan 450007, P. R. China

[b]College of Chemistry and Chemical Engineering, Henan Institute of Science and Technology, Xinxiang, Henan 453000, P. R. China

## Contents

1.General Method

Characterization

Powder X-ray diffraction (PXRD) was executed with the Bruker D8 Advance X-ray diffractometer with Cu $K_{\alpha 1}$. X-ray photoelectron spectroscopy (XPS) spectra were measured by a ThermoFisher Scientific K-Alpha X-ray photoelectron spectroscopy with Al-Kα X-ray source. spectra of all the samples were recorded using a Bruker-ALPHA spectrophotometer with KBr pellets in 400-4000 cm^{-1} region. UV-vis absorption spectra were obtained on a PerkinElmer Lambda 950 spectrophotometer. The Zeta potential of the powder sample film was measured using the Malvern Zetasizer Nano ZS nanoparticle size and Zeta potential analyzer (DLS). Electrochemical impedance spectroscopy (EIS) measurements were performed via the CHI660E electrochemical workstation (Shanghai Chenhua Apparatus) using a conventional three-electrode cell (saturated silver electrode as the reference electrode, Pt plate as the auxiliary electrode), and Na_2SO_4 solution (0.2 mol L^{-1}) was employed as the electrolyte. The surface roughness images of the films were measured by atomic force microscopy (AFM), and the surface potential of the sample films was carried out by the Kelvin probe force microscopy (KPFM) mode on the Bruker Dimension Icon. The short circuit current (I_{sc}) was tested by a SR570 low-noise current amplifier (Stanford Research System) and the output voltage (V_{oc}) was tested by a high voltage test system for nanogenerator with BIV-26A (Keithley a Tektronix Company with 2657A high power system sourceMeter). The device operating parameters of 5 Hz frequency, 3.5 N load, and 3 cm separation distance were employed for all TENGs, unless specified.

2. Procedure for the light-induced copper-catalyzed C-C cross-coupling reactions using a Cu^I-MOF-TENG device.

The mixture solution of potassium carbonate (0.52 mmol), phenylacetylene (**1**, 0.6 mmol), aromatic iodides (**2a-j**, 0.5 mmol), catalyst (**Cu^I-MOF**, 10 mol %), methanol (2 mL) and acetonitrile (2 mL) was sealed tightly and stirred under irradiation of 14 blue LEDs (1 W) driven by the **Cu^I-MOF-TENG** device. The reaction temperature was maintained at 25-28 °C. After approximately 10 hours, the reaction mixture was cooled, filtrated, and purified, respeectively.
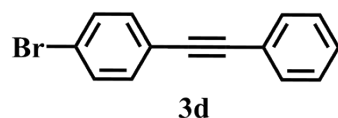

3a
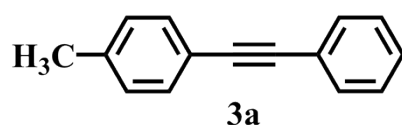
1-methyl-4-(phenylethynyl)benzene: The product is obtained as colorless solid (isolated yield: 91 %). This compound had been reported.^{1}H NMR (400 MHz, CDCl₃) δ 7.55-7.50 (m, 2H), 7.46-7.41 (m, 2H), 7.37-7.31 (m, 3H), 7.19-7.13 (m, 2H), 2.37 (s, 3H).
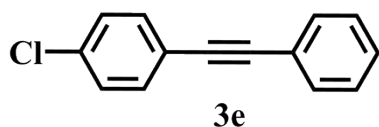

3b
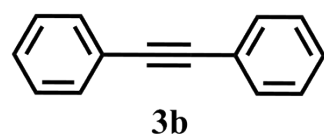
Diphenylacetylene: The product is obtained as colorless solid (isolated yield: 91 %). This compound had been reported.^{1}H NMR (400 MHz, CDCl₃) δ 7.60-7.49 (m, 4H), 7.42-7.29 (m, 6H).
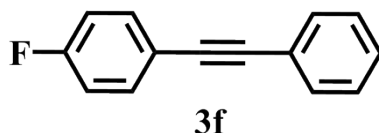

3c
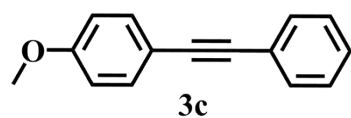
1-methoxy-4-(phenylethynyl)benzene: The product is obtained as colorless solid (isolated yield: 88 %). This compound had been reported.^{1}H NMR (400 MHz, CDCl₃) δ 7.57-7.42 (m, 4H), 7.39-7.29 (m, 3H), 6.92-6.82 (m, 2H), 3.83 (s, 3H).
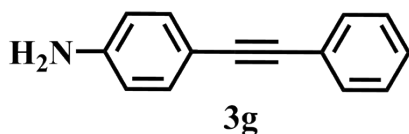

3d

1-bromo-4-(phenylethynyl)benzene: The product is obtained as colorless solid (isolated yield: 87 %). This compound had been reported.[1] ^{1}H NMR (400 MHz, CDCl₃) δ 7.57-7.45 (m, 4H), 7.43-7.31 (m, 5H).
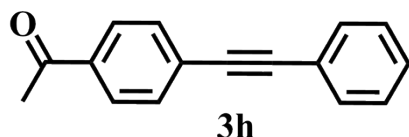
3e

1-Chloro-4-(phenylethynyl)benzene: The product is obtained as colorless solid (isolated yield: 86 %). This compound had been reported.[2] ^{1}H NMR (400 MHz, CDCl3) δ 7.59-7.42 (m, 4H), 7.42-7.29 (m, 5H).
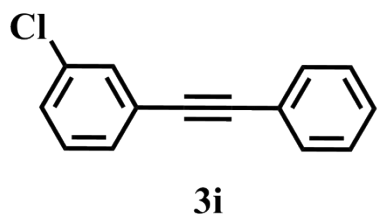

3f

1-fluoro-4-(2-phenylethynyl)benzene: The product is obtained as colorless solid (isolated yield: 88 %). This compound had been reported.[2] ^{1}H NMR (400 MHz, CDCl$_3$) δ 7.53 (dddt, J = 10.0, 8.2, 5.1, 2.7 Hz, 4H), 7.43 – 7.30 (m, 4H), 7.11 – 7.00 (m, 1H).
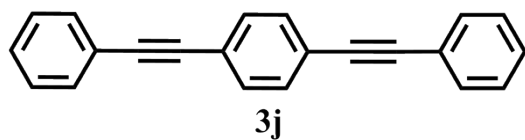

3g

4-(Phenylethynyl)aniline: The product is obtained as colorless solid (isolated yield: 91 %). This compound had been reported.[3] ^{1}H NMR (400 MHz, CDCl$_3$) δ 7.56-7.44 (m, 2H), 7.41-7.27 (m, 5H), 6.70-6.59 (m, 2H), 3.82 (s, 2H).

3h

1-[4-(2-phenyleth-1-ynyl)phenyl]ethan-1-one: The product is obtained as colorless solid (isolated yield: 90 %). This compound had been reported.[2] ^{1}H NMR (400 MHz, CDCl$_3$) δ 7.98-7.91 (m, 2H), 7.65-7.51 (m, 4H), 7.37 (h, J = 1.9 Hz, 3H), 2.62 (s, 3H).

3i

1-(3-Chlorophenyl)-2-phenylethyne: The product is obtained as colorless solid (isolated yield: 89 %). ^{1}H NMR (400 MHz, CDCl$_3$) δ 7.54 (dp, J = 5.9, 2.3 Hz, 3H), 7.44-7.26 (m, 6H).

3j

1,4-Bis(phenylethynyl)benzene: The product is obtained as colorless solid (isolated yield: 88 %). This compound had been reported.[2] ^{1}H NMR (400 MHz, CDCl$_3$) δ 7.63-7.46 (m, 8H), 7.36 (dq, J = 4.8, 2.4 Hz, 6H).

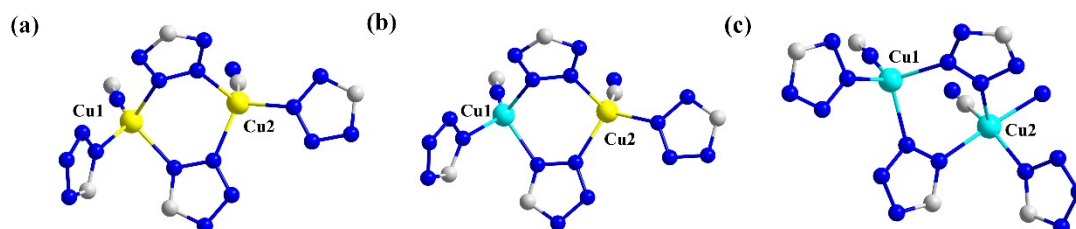# 3.Additional characterizations for Cu^I-MOF, Cu^{I}Cu^{II}-MOF and Cu^{II}-MOF.

Fig. S1. Coordination environment of Cu-MOFs: (a) **Cu^I-MOF**, (b) **Cu^{I}Cu^{II}-MOF**, and (c) **Cu^{II}-MOF**, respectively. Hydrogen atoms were omitted for clarity.
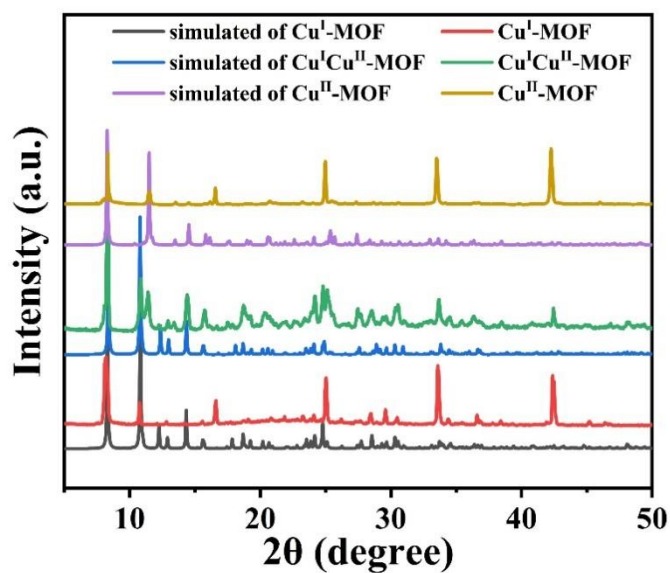

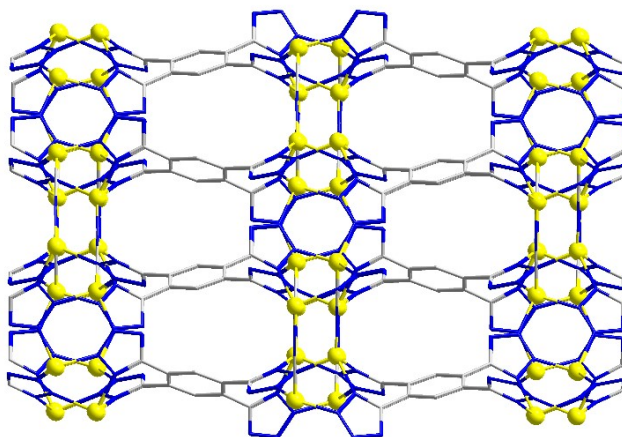**Fig. S2.** PXRD patterns of **Cu^I-MOF**, **Cu^{I}Cu^{II}-MOF** and **Cu^{II}-MOF**.

Fig. S3. A view of the 3D network of **Cu^I-MOF**.
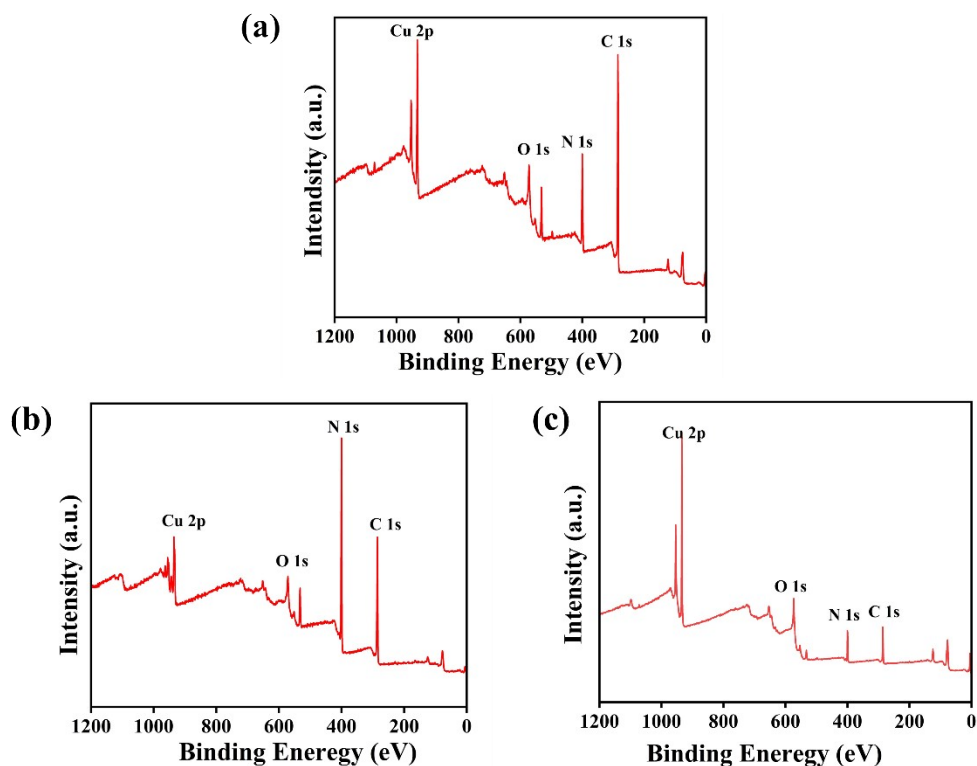
Fig. S4. XPS spectra of (a) **Cu^{I}-MOF**, (b) **Cu^{I}Cu^{II}-MOF**, and (c) **Cu^{II}-MOF**, respectively.
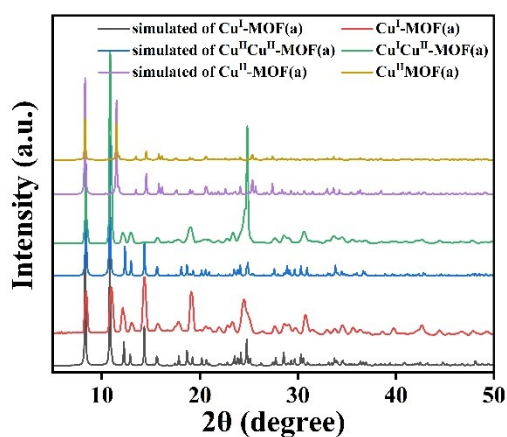
Fig. S5. PXRD spectrum of **Cu^{I}-MOF(a)**, **Cu^{I}Cu^{II}-MOF(a)**, and Cu^{II}-MO**F(a)**, respectively.
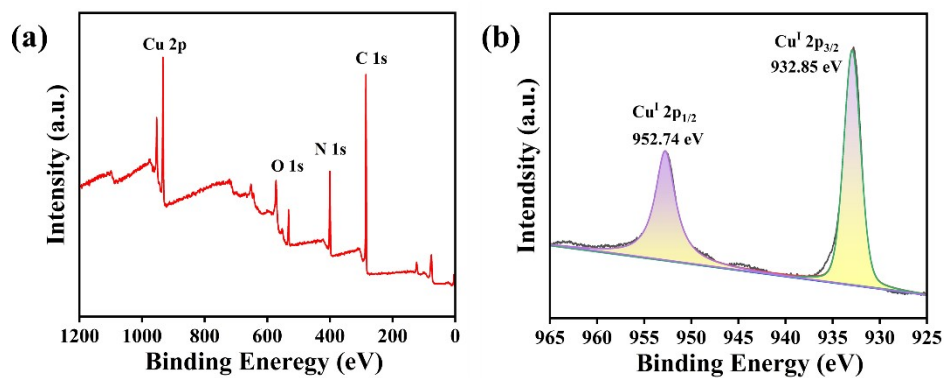
Fig. S6. (a, b) XPS spectra of **Cu^{I}-MOF (a)**.
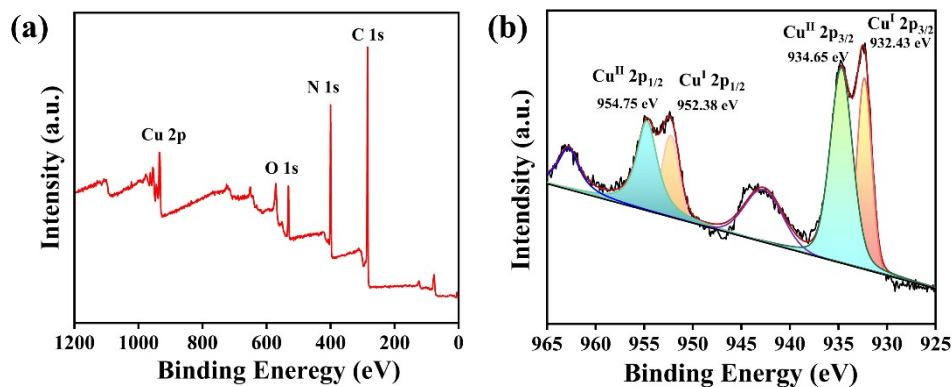
Fig. S7. (a, b) XPS spectra of **Cu^{I}Cu^{II}-MOF(a)**.
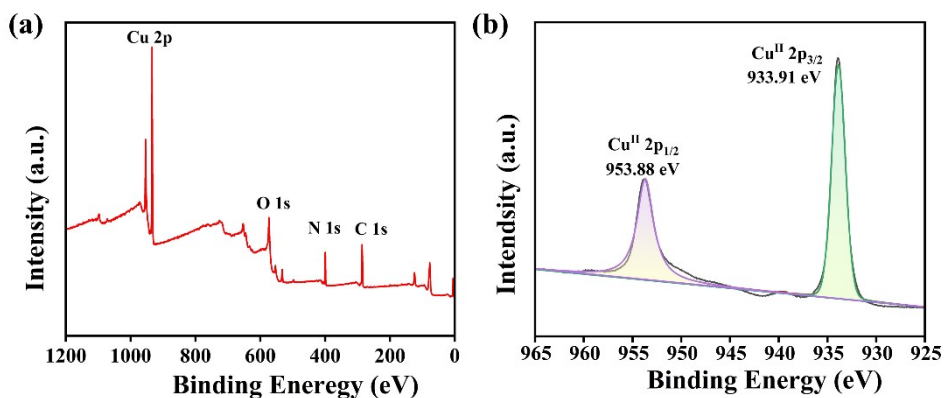
Fig. S8. (a, b) XPS spectra of **Cu^{II}-MOF(a)**.
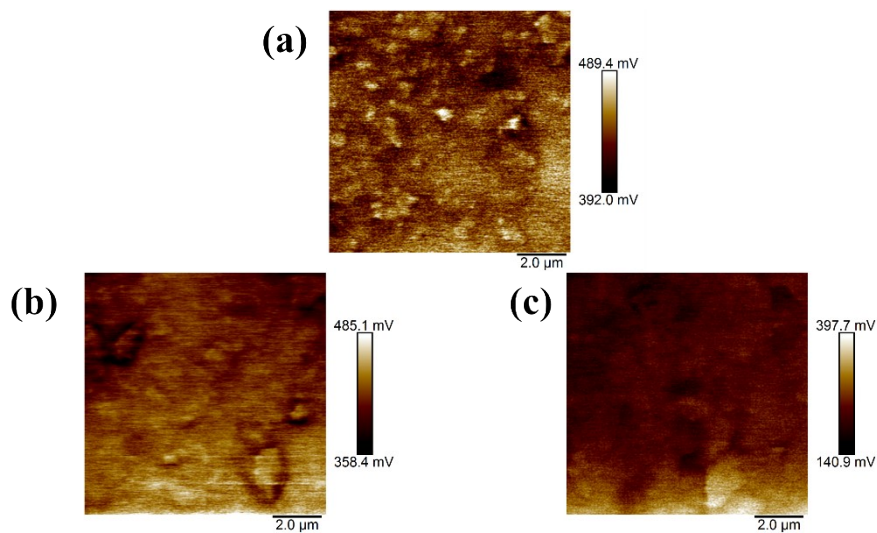
Fig. S9. The KPFM images of (a) **Cu^I-MOF**, (b) **Cu^{I}Cu^{II}-MOF**, and (c) **Cu^{II}-MOF**, respectively.
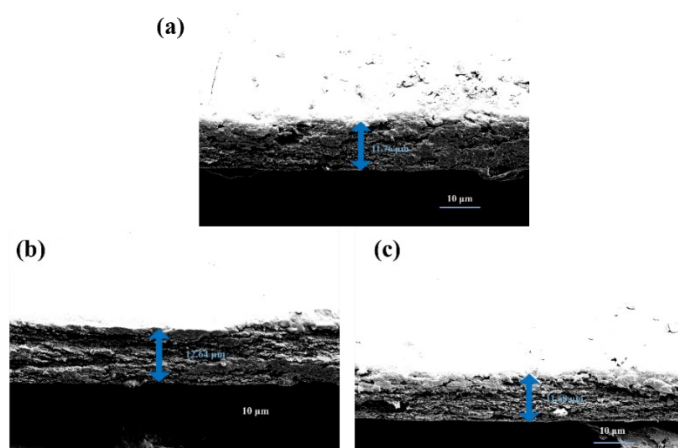
Fig. S10. Cross-sectional SEM images of the samples: (a) **Cu^{I}-MOF**, (b) **Cu^{I}Cu^{II}-MOF**, (c) **Cu^{II}-MOF**.
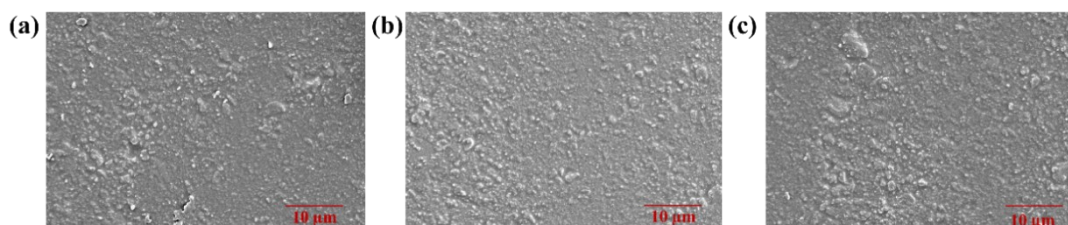
Fig. S11. The SEM images of the samples before collision: (a) **Cu^{I}-MOF**, (b) **Cu^{I}Cu^{II}-MOF**, (c) **Cu^{II}-MOF**.
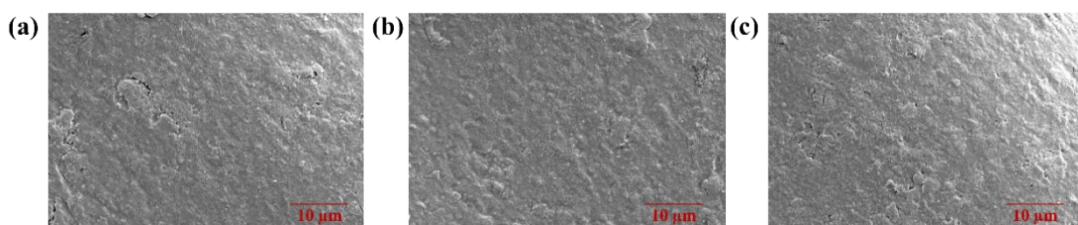
Fig. S12. The SEM images of the samples after collision: (a) **Cu^{I}-MOF**, (b) **Cu^{I}Cu^{II}-MOF**, (c) **Cu^{II}-MOF**.
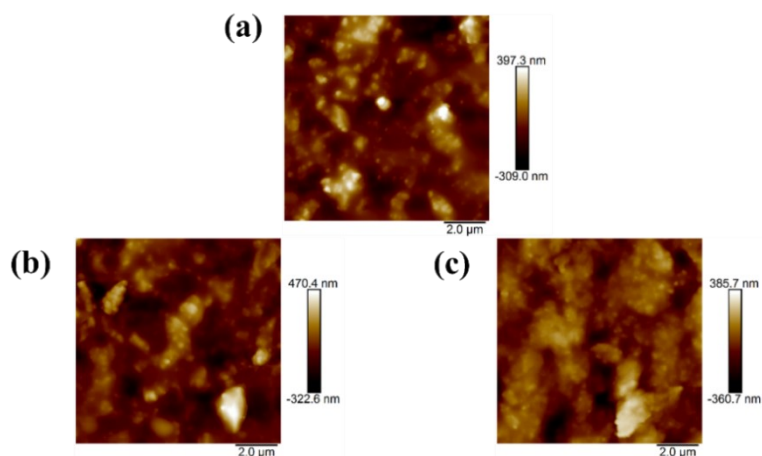
Fig. S13. The AFM images of the samples (a) **Cu^{I}-MOF**, (b) **Cu^{I}Cu^{II}-MOF**, (c) **Cu^{II}-MOF**.

4.Additional characterizations of Cu^I-MOF-TENG, Cu^{I}Cu^{II}-MOF-TENG and Cu^{II}-MOF-TENG.

The Triboelectric Nanogenerator (TENG) works on triboelectrification and electrostatic induction. Initially (Fig. S14(i)), different - material friction layers in close contact transfer electrons at the interface, creating opposite-charged surfaces for internal electrostatic balance. As they separate (Fig. S14(ii)), electrostatic induction induces opposite-sign charges on electrodes. Increasing separation boosts induced charges and electrode potential difference, driving external-circuit current. At maximum separation (Fig. S14(iii)), induced charges and potential difference peak; external - circuit current stabilizes for power output. During re-contact (Fig. S14(iv)), induced charges and potential difference drop; current reverses. This cycle repeats, with TENG converting mechanical energy to electrical energy via friction-layer contact-separation for external-circuit power supply.
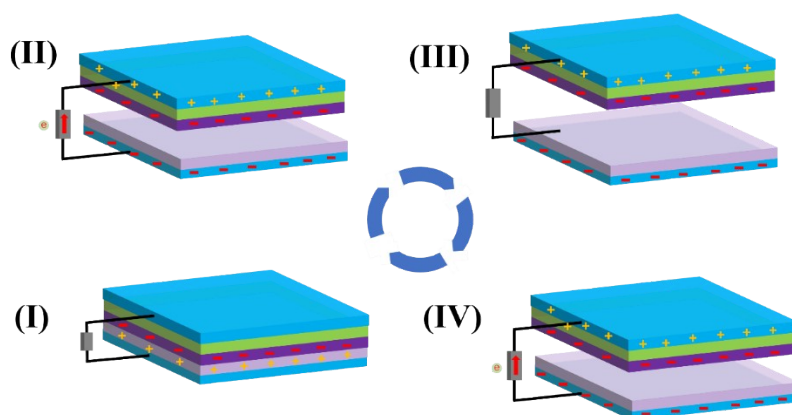

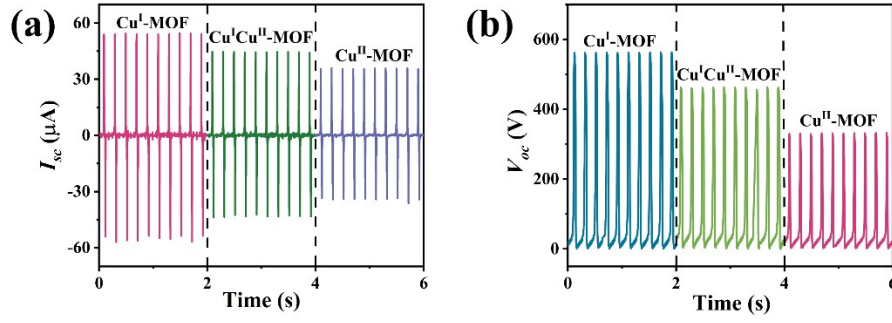**Fig. S14.** Mechanism of operation of Cu-MOF-based-TENGs.

Fig. S15. (a) I_{sc} of the **Cu^I-MOF-TENG**, **Cu^{I}Cu^{II}- MOF-TENG**, and **Cu^{II}- MOF-TENG** at 5 Hz, respectively. (b) V_{oc} of the **Cu^I-MOF -TENG**, **Cu^{I}Cu^{II}-MOF-TENG**, and **Cu^{II}- MOF-TENG** at 5 Hz, respectively.
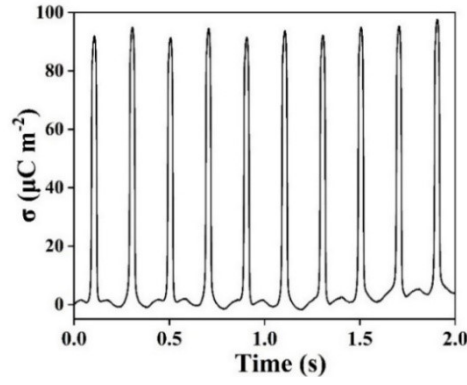

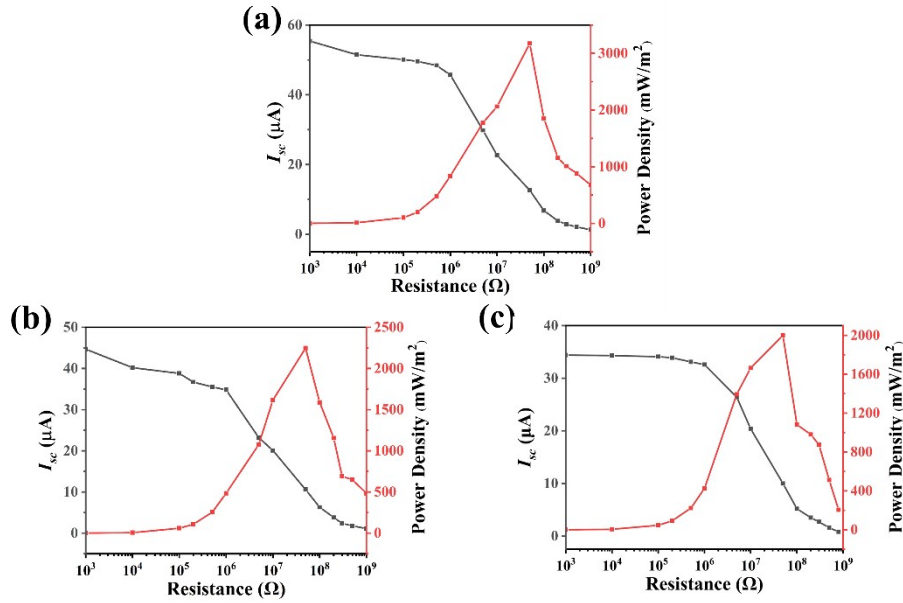**Fig. S16**.Charge density of **Cu^I-MOF-TENG**.

Fig. S17. I_{sc} and power density of Cu-MOF-based-TENG under different external load resistance: (a) **Cu^I-MOF-TENG**, (b) **Cu^{I}Cu^{II}-MOF-TENG**, and (c) **Cu^{II}-MOF-TENG**, respectively.

Table S1. Compared with the reported of MOF -based TENG Outputs

| MOF-based TENG	Device size (cm²)	Voltage (V)	Current (µA)	Power density (µW/cm²)	Ref.
ZIF-67/PVDF	2 × 2	119.6	7.7	171	4
ZIF-8@ZnO Nanosheets	5 × 5	200.5	41.5	80	5
NF-MOF/PDMS	2 × 2	215	10	263	6
MAP1-18/PTFE	5.5 × 5.5	796	46	148	7
PVA@ZIF-67//PET	10 × 10	300	47.5	59.3	8
ZIF-7//Kapton	2.5 × 2.5	60	1.1	0.77	9
Cd-MOF/PDMS/Cu	2 × 3	193.4	0.86	12.4	10
MOF-5	2.5 × 2.5	484	40	508	11
PVA@ZIF-67//PET	10 × 10	300	47.5	59.3	12
Co-CP//PVDF	5 × 5	350	37	120	13
Cu^I-MOF//PVDF	**5 × 5**	**558.0**	**53.71**	**316.63**	**This work**
Cu^I Cu^{II} -MOF//PVDF	**5 × 5**	**465.49**	**43.93**	**224.42**	**This work**
Cu^{II}-MOF//PVDF	**5 × 5**	**329.45**	**35.67**	**200.0**	**This work**
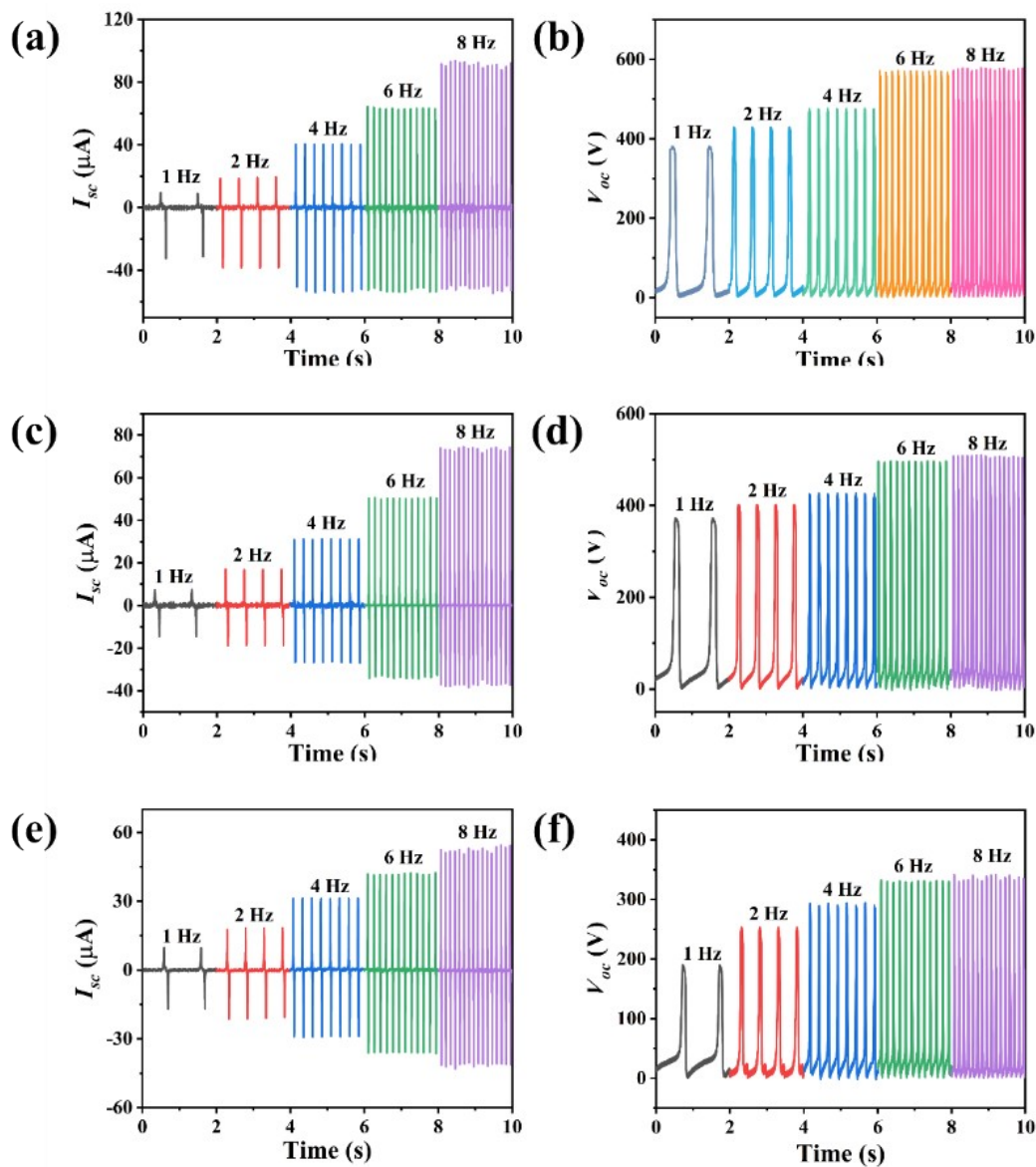
Fig. S18. I_{sc} and V_{oc} of Cu-MOF-based-TENG under different operating frequencies: (a-b) **Cu^I-MOF-TENG**, (c-d) **Cu^ICu^{II}-MOF-TENG**, (e-f) **Cu^{II}-MOF-TENG**, respectively.
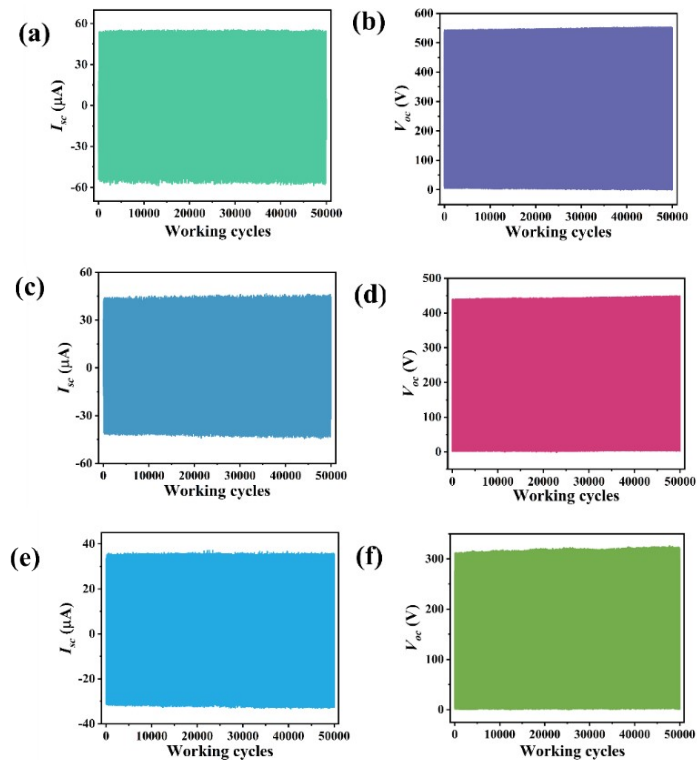
Fig. S19. I_{sc} and V_{oc} of Cu-MOF-based-TENG in vacuum after working 50,000 cycles: (a-b) **Cu^I-MOF-TENG**, (c-d) **Cu^{I}Cu^{II}-MOF-TENG**, (e-f) **Cu^{II}-MOF-TENG**, respectively.
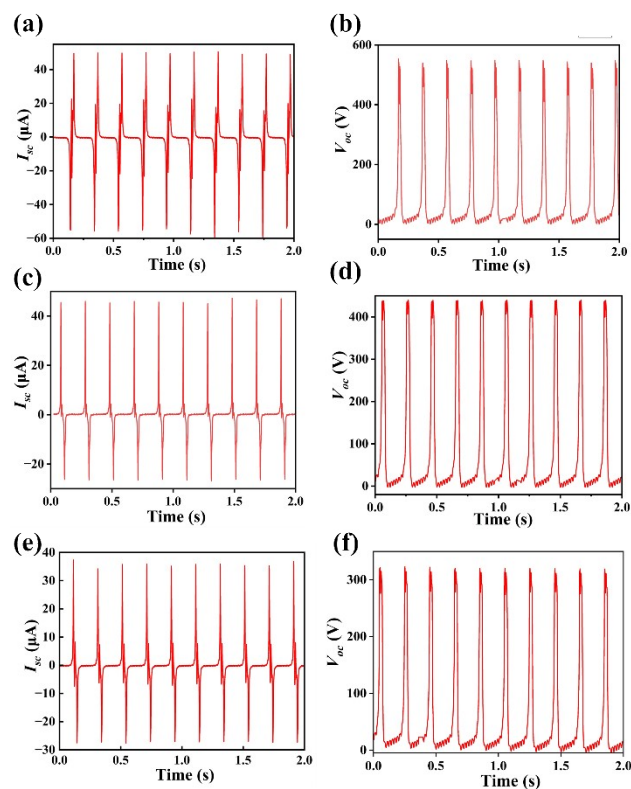
Fig. S20. I_{sc} and V_{oc} of Cu-MOF-based-TENG after fabrication two months. (a-b) **Cu^I-MOF-TENG**, (c-d) **Cu^{I}Cu^{II}-MOF-TENG**, (e-f) **Cu^{II}-MOF-TENG**, respectively.
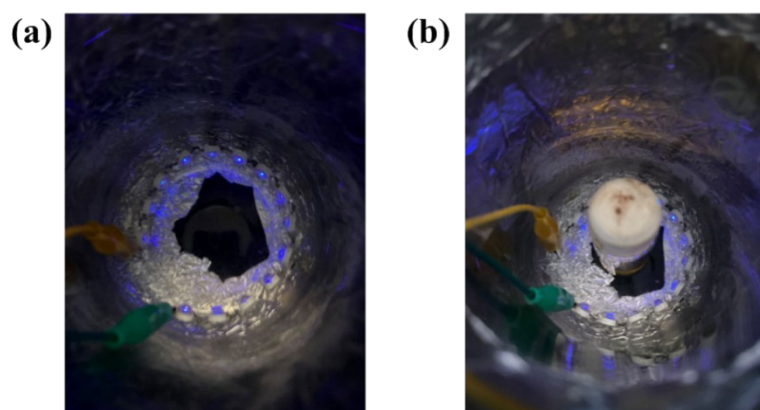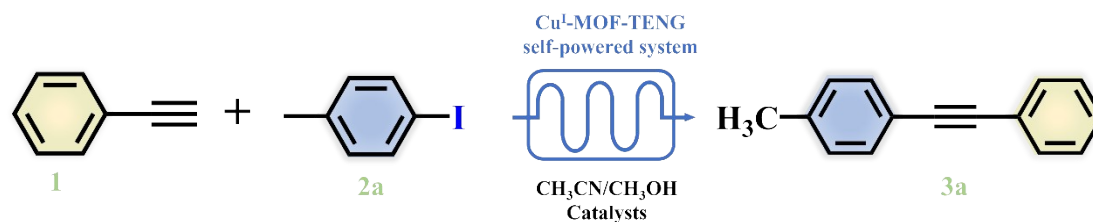
Fig. S21. The digital photograph of 14 LED beads powered by the **Cu^I-MOF-TENG**.

Table S2. Optimization of photocatalytic C-C cross-coupling reactions using a **Cu^I-MOF-TENG** device ^{a}.

Entry	Catalysts (mol%)	Light	Time (h)	BHT/TEMPO	Yield (%) ^{b}
1	Cu^I-MOF (10)	+	10	-	91
2	Cu^{I}Cu^{II}-MOF (10)	+	10	-	75
3	Cu^{II}-MOF (5)	+	10	-	55
4	Cu^I-MOF (5)	+	2	-	25
5	Cu^I-MOF (5)	+	4	-	55
6	Cu^I-MOF (5)	+	8	-	67
7	Cu^I-MOF (5)	+	10	-	79
8	Cu^I-MOF (5)	+	12	-	78
9	Cu^I-MOF (15)	+	10	-	92
10	Cu^I-MOF (15)	-	10	-	n.r
11	/^{c}	+	10	-	trace
12	Cu^I-MOF (10)	+	10	+	45

^{a} Phenylacetylene (**1**, 0.6 mmol), 4-Iodotoluene (**2a**, 0.5 mmol), catalyst (**Cu^I-MOF**, 10 mol %), potassium carbonate (0.52 mmol), methanol (2 mL) and acetonitrile (2 mL). ^{b} Isolated Yield of the product **3a** after 10 hours. ^{c} Without the catalysts.

To further initiate the practical application with the high outputs of **Cu^I-MOF-TENG**, 14 blue lamp beads (465 nm, 1 W) with connection in series were directly powered by **Cu^I-MOF-TENG** to provide visible light irradiation (Fig. S21), which was employed as visible light source to execute the photocatalytic reaction by using Cu-MOFs as catalysts, fabricating a self-powered photocatalytic continuous-flow coupling system. As a consequence of such photocatalytic system, we were inclined to integrate the catalytic advantages of MOFs to obtain selective catalysis with outstanding yields, and on the other, combine the **Cu^I-MOF-TENG** device as a sustainable and green energy source to drive blue lamp beads, so that the bifunctional advantage of MOFs-based TENG and catalysts was built, thereby generating an efficient self-powered

photocatalytic system with the bifunctional MOFs. The cross-coupling reaction of phenylacetylene (**1**) and 4-iodotoluene (**2a**) was chosen as the model substance with which to explore this reaction conditions. The standard conditions comprised the use of **Cu^I-MOF** as catalyst in combination with K_2CO_3 in methanol/acetonitrile (MeOH/MeCN) and under blue LEDs irradiation, which was generated by **Cu^I-MOF-TENG**. The desired product (**3a**) was achieved with good selectivity and yield (91 %, Table S2, entry 1). It was seen that the replacement of catalyst **Cu^I-MOF** with **Cu^{I}Cu^{II}-MOF** or **Cu^{II}-MOF** led to decrease the yield of **3a** (75 % or 55 %, Table S2, entries 2-3). Meanwhile, different reaction times were evaluated and it was found that a time of 10 hours provided the best yield and selectivity (Table S2, entries 4-8). When 0.15 mmol catalyst **Cu^I-MOF** replaced 0.10 mmol, a similar activity and yield of 92 % was accomplished but 0.05 mmol catalyst **Cu^I-MOF** furnished the desired product **3a** in only 79 % yield (Table S2, entry 9). In the absence of the light irradiation or catalysts, no **3a** was obtained, indicating that both were necessary for this self-powered photocatalytic system (Table S2, entries 10-11). In addition, adding butylated hydroxytoluene (BHT) or 2,2,6,6-tetramethylpiperidine-1-oxo (TEMPO) to the photocatalytic system resulted in a yield of 45 % for 3a (Table S2, entry 12). Thus, the self-powered selective photocatalytic continuous-flow coupling reaction could execute smoothly with **Cu^I-MOF** blue-light irradiation as the standard condition.
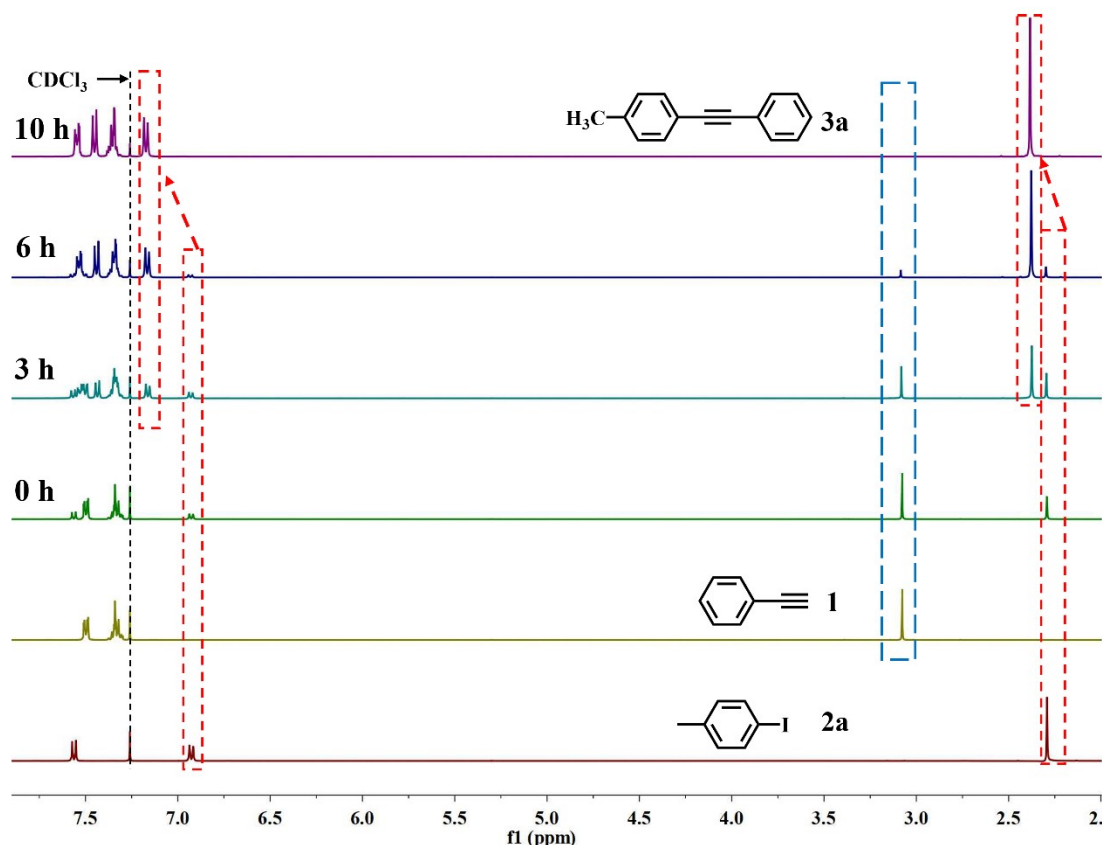
Fig. S22. ^{1}H NMR spectra of **1** to **3a** after visible light irradiation for 0, 5 and 10 h, respectively.

The self-powered selective photocatalytic c continuous-flow coupling process was investigated with **1** and **2a** by ^{1}H NMR spectroscopy monitoring under the standard reaction conditions. It was found that the hydrogen signal of the alkyne group (-C≡CH) (δ = 3.10 ppm) was gradually vanished, suggesting that the photocatalytic coupling process was proceeded smoothly (Fig. S22). After blue-light irradiation 3 h, the methyl (-CH$_3$) and methylene (-CH$_2$-) hydrogen signals of **2a** were clearly shifted. Thus, these results verified that the self-powered selective photocatalytic continuous-flow coupling process was performed. With the extension of irradiation time, the singlet hydrogen of alkyne peak weakened, and the correspondingly multiple hydrogen signals promptly strengthened. Finally, the selective photocatalytic cross-coupling process was fully achieved when the blue-light irradiation was 10 h, confirmed by the variation of hydrogen peaks.

Table S3. Comparison of optimized photocatalytic C-C cross coupling reaction between standard Sonogashira coupling and **Cu^I-MOF-TENG** device
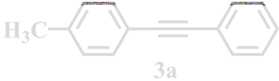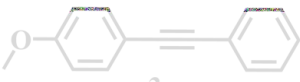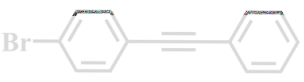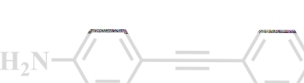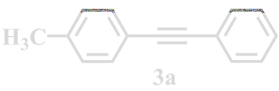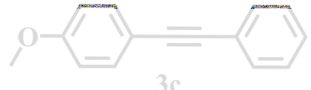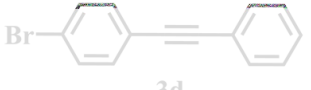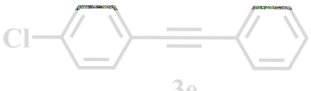
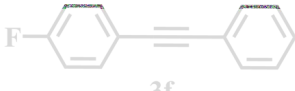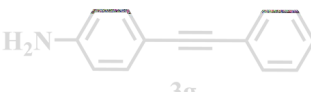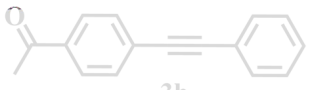| Entry	Catalysts (mol%)	product	Traditional reaction yield (%)	This work yield (%)	Ref.
1	Cu$_2$O TNCs	3a	89	**91**	2
2	Cu$_2$O TNCs	3b	89	**91**	2
3	CuCl	3c	82	**88**	3
4	CuCl	3d	91	**87**	3
5	Cu$_2$O TNCs	3e	80	**86**	2
6	Cu$_2$O TNCs	3f	81	**88**	2
7	CuCl-Ag(OTf)	3g	88	**91**	3
8	CuCl-Ag(OTf)	3h	80	**90**	3
9	Cu$_2$O TNCs	3j	88	**88**	2

Table S4. Optimization of photocatalytic C-C cross-coupling reactions without catalysts using a **Cu^I-MOF-TENG** device.

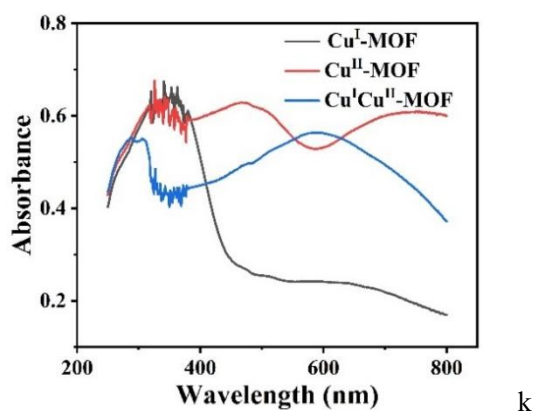| Entry	Catalysts (mol%)	product	yield (%)
1	/	3a	trace
2	/	3b	trace
3	/	3c	trace
4	/	3d	trace
5	/	3e	trace
6	/	3f	trace
7	/	3g	trace
8	/	3h	trace
9	/	3j	trace

Fig. S23. UV-vis diffuse reflectance spectra of **Cu^I-MOF**, **Cu^{I}Cu^{II}-MOF** and **Cu^{II}-MOF**.
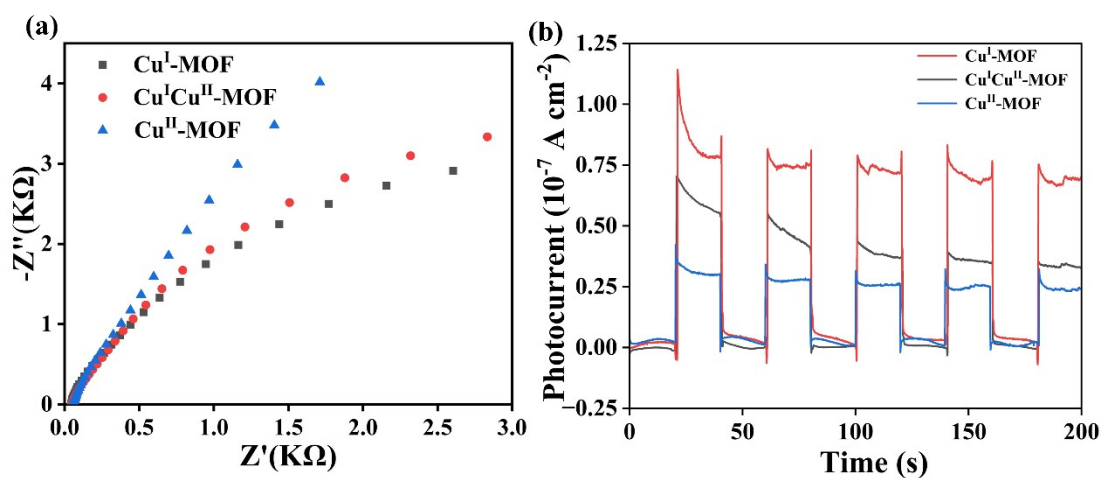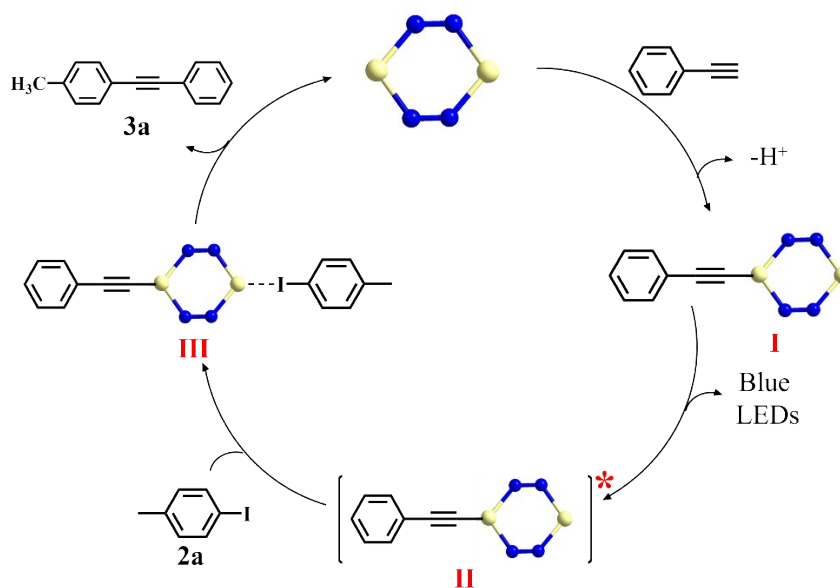

Fig. S24. (a) EIS for **Cu^I-MOF**, **Cu^{I}Cu^{II}-MOF** and **Cu^{II}-MOF**. (b) The photocurrent response for **Cu^I-MOF**, **Cu^{I}Cu^{II}-MOF** and **Cu^{II}-MOF**.

Scheme 1. Mechanistic study of the photocatalytic C-C cross-coupling reactions using a **Cu^I-MOF-TENG** device.
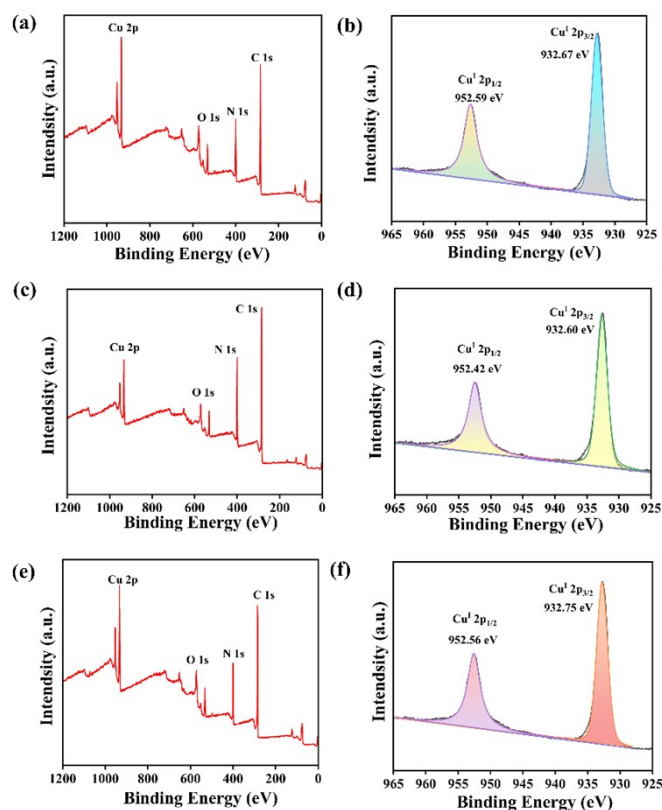
Fig. S25. (a, b) XPS spectrum of **Cu^I-MOF** before solvent resistance test. (c, d) XPS spectrum of **Cu^I-MO**F after 5 h solvent resistance test. (e, f) XPS spectrum of **Cu^I-MOF** after 10 h solvent resistance test.

To better clarify the variations of the microenvironment for the active sites during the selective photocatalytic cross-coupling process, XPS was employed to assess the cross-coupling process at different reaction times (0, 5, and 10 h) (Fig. S25 a-f). The Cu $2p_{3/2}$ peaks at 932.67 (0 h), 932.60 (5 h) 9532.75 eV (10 h), respectively, and the corresponding and Cu $2p_{1/2}$ peaks at 952.59 eV (0 h), 952.42 eV (5 h) and 952.56 eV (10 h), respectively, confirmed that Cu maintained their monovalence Cu^I states in **Cu^I-MOF** throughout the reaction process. Thus, the XPS results displayed that the microenvironment of the active sites in **Cu^I-MOF** was kept and that these sites could continue to realize the selective photocatalytic cross-coupling reaction.
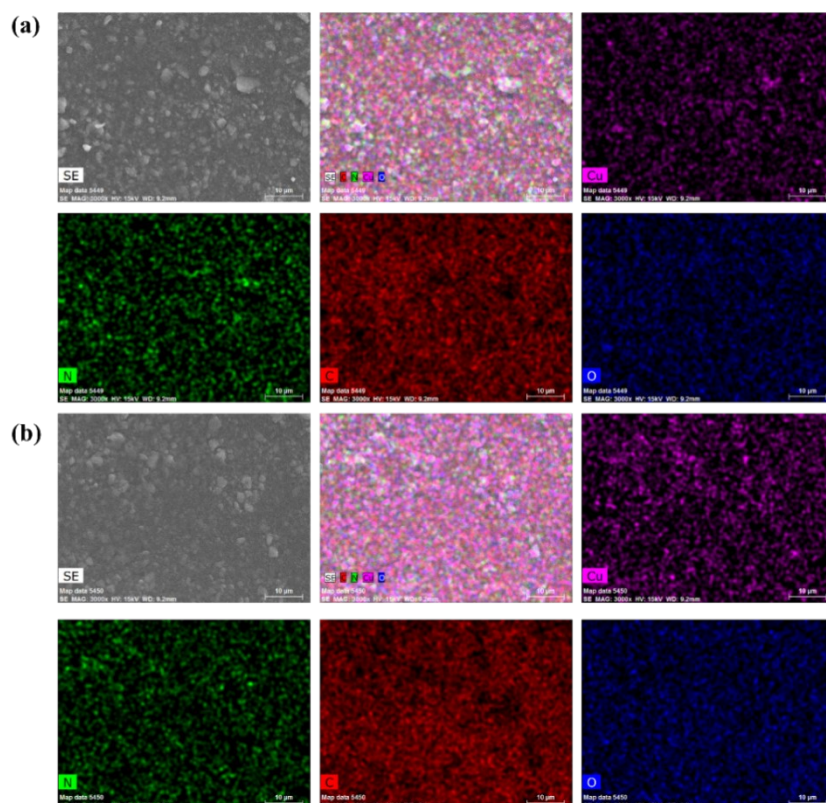
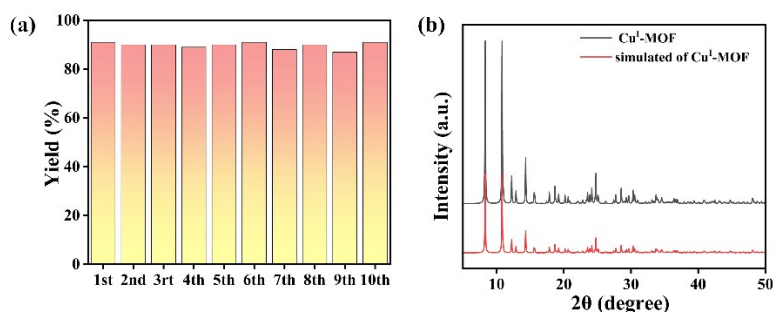**Fig. S26.** SEM and Elemental mapping images of **Cu^I-MOF** (a) before and (b) after photocatalytic reactions.


Fig. S27. (a) Yields after ten cycles of **Cu^I-MOF**. (b) PXRD patterns of **Cu^I-MOF** after recycling.

In addition, the efficiently photocatalytic activity and selectivity of **Cu^I-MOF** encourage us to explore its heterogeneous characterwastics. The ICP-AES experiments displayed that very little Cu leaching was achieved (0.49 ppm from the **Cu^I-MOF**). Then, the hot filtration measurement for this selective photocatalytic cross-coupling process was investigated with **2a**, which indicated that 32 % **2a** was converted to the desired product **3a** by employing **Cu^I-MOF** as photocatalyst in 1 h. After that, **Cu^I-MOF** was isolated from the reaction system to produce the mother solution for reacting another 9 h. It could be seen that the cross-coupling process was completely inhibited,

suggesting that this selective photocatalytic cross-coupling process did not execute in absence of photocatalyst **Cu^I-MOF**. Furthermore, SEM and mapping tests revealed that the morphology structures and elemental distributions (Cu, N, O, and C) for photocatalyst **Cu^I-MOF** were resemblance to those before the reaction (Fig. S26). Accordingly, these results evidently proved that photocatalyst **Cu^I-MOF** was an actually heterogeneous catalyst. In addition, the reusability property of photocatalyst **Cu^I-MOF** was examined by the sequential experiments, which indicated that the activity and selectivity of **Cu^I-MOF** were no apparent attenuation after 10 runs continuous experiments, revealing that **Cu^I-MOF** possessed the superiorly stable capacity during the consecutive reaction processes (Fig. S27(a)). The XPS and PXRD results indicated that the framework of the recoverable **Cu^I-MOF** was well matched with the initial structure, suggesting photocatalyst **Cu^I-MOF** with a prominent selectivity and efficiency to implement cross-coupling process after at least 10 runs (Fig. S27(b)).
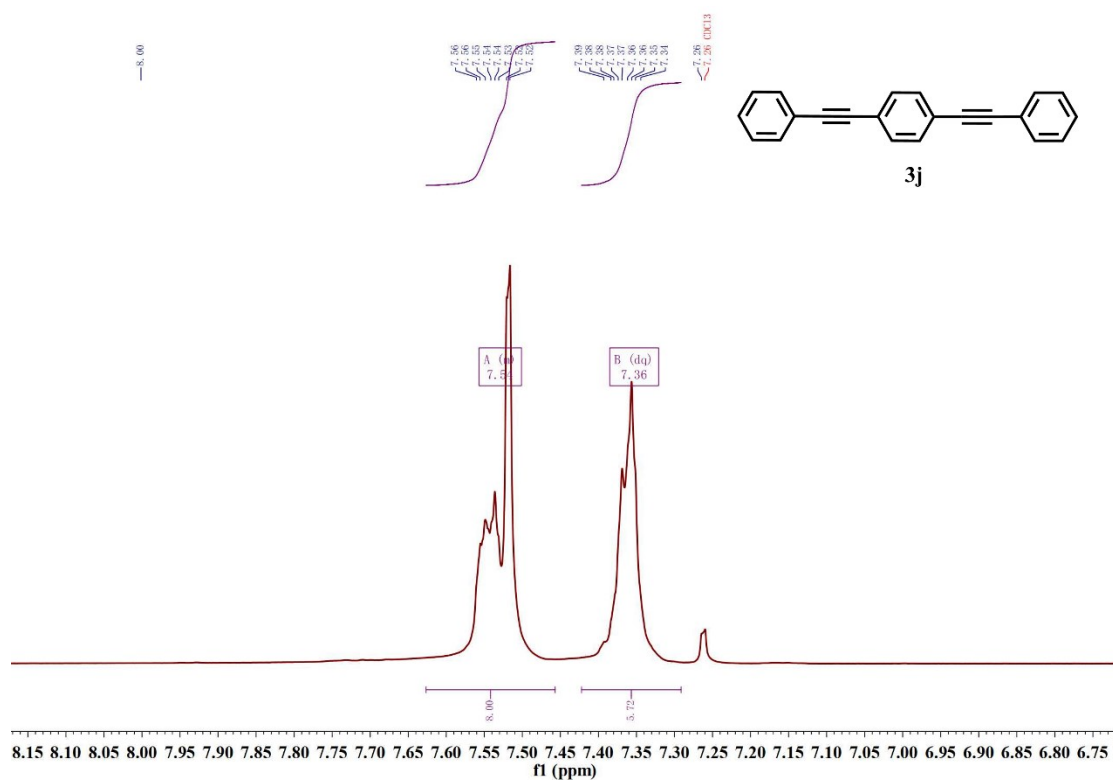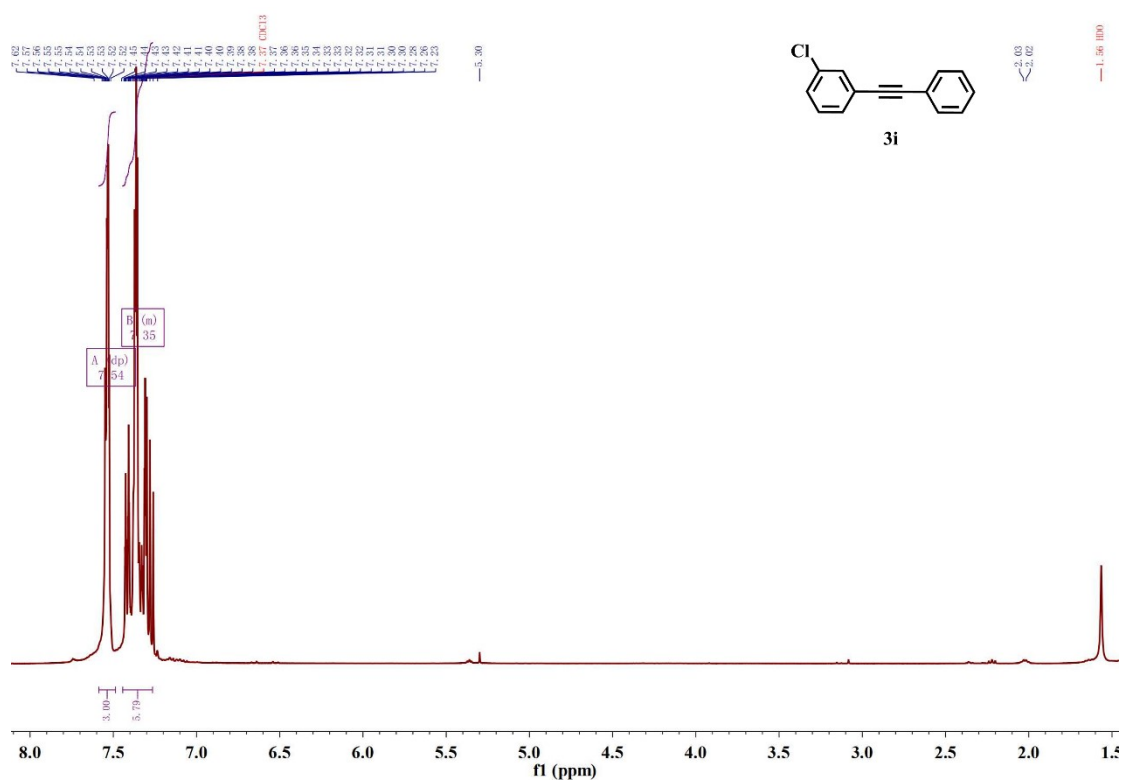
5.Spectral copies of ^{1}H NMR of compounds obtained in this study.

3a

3b
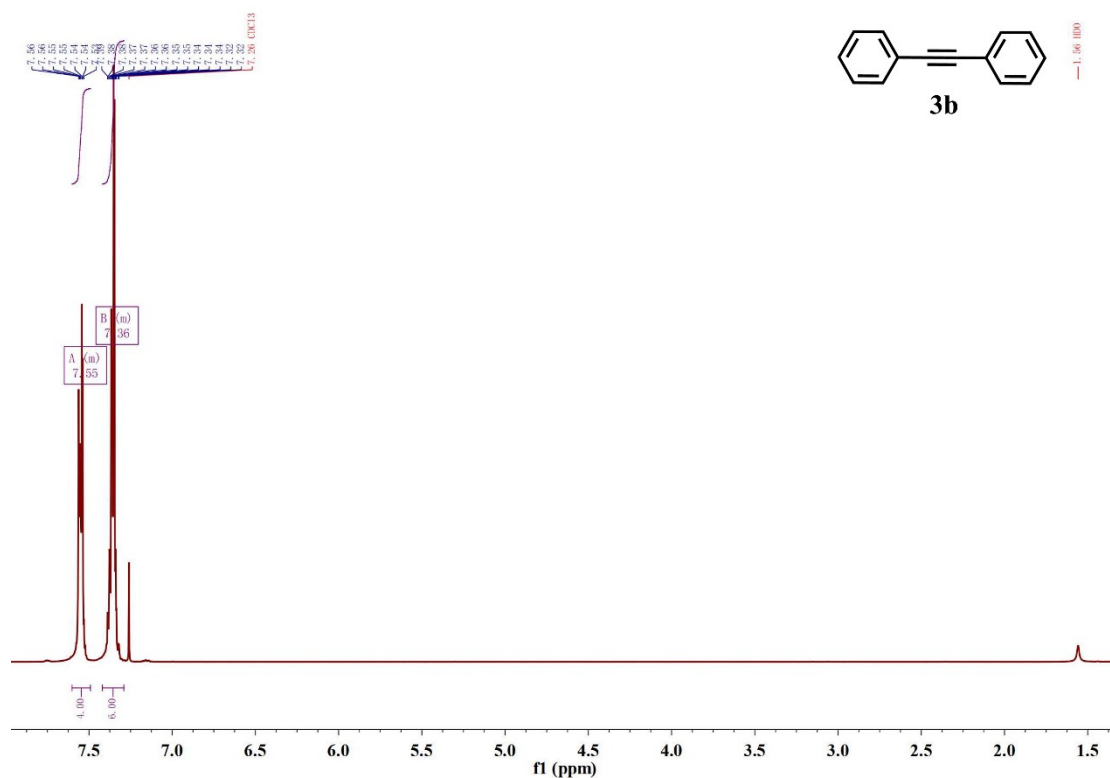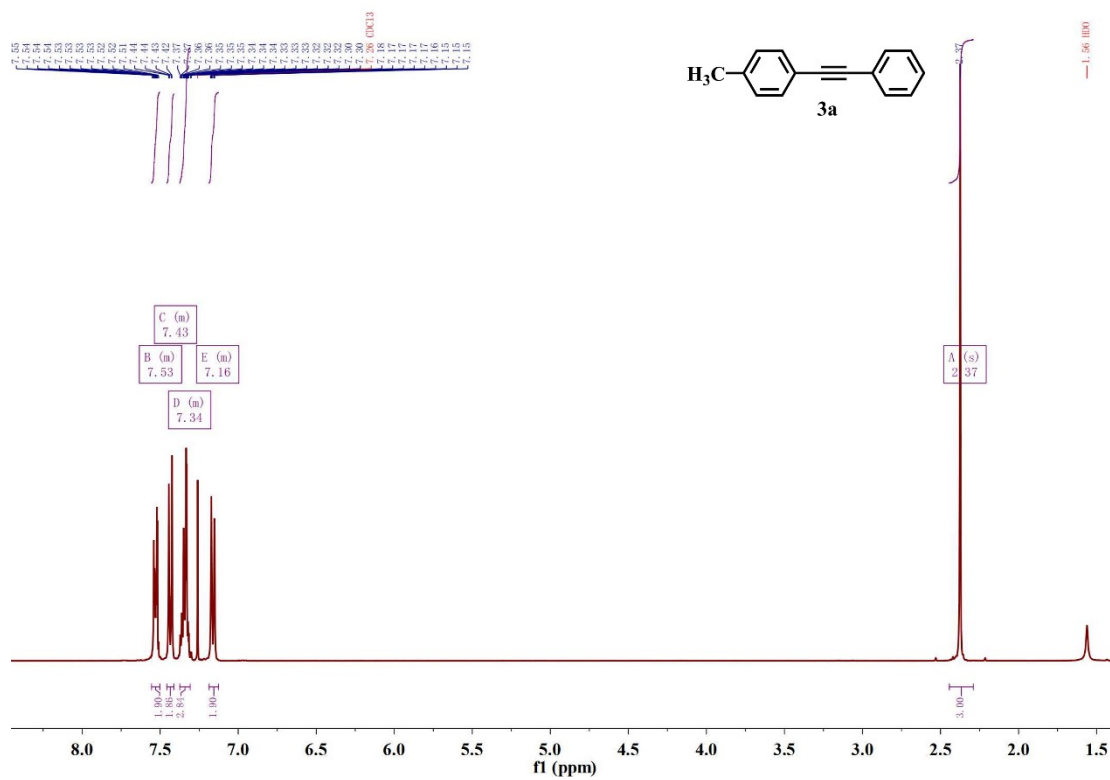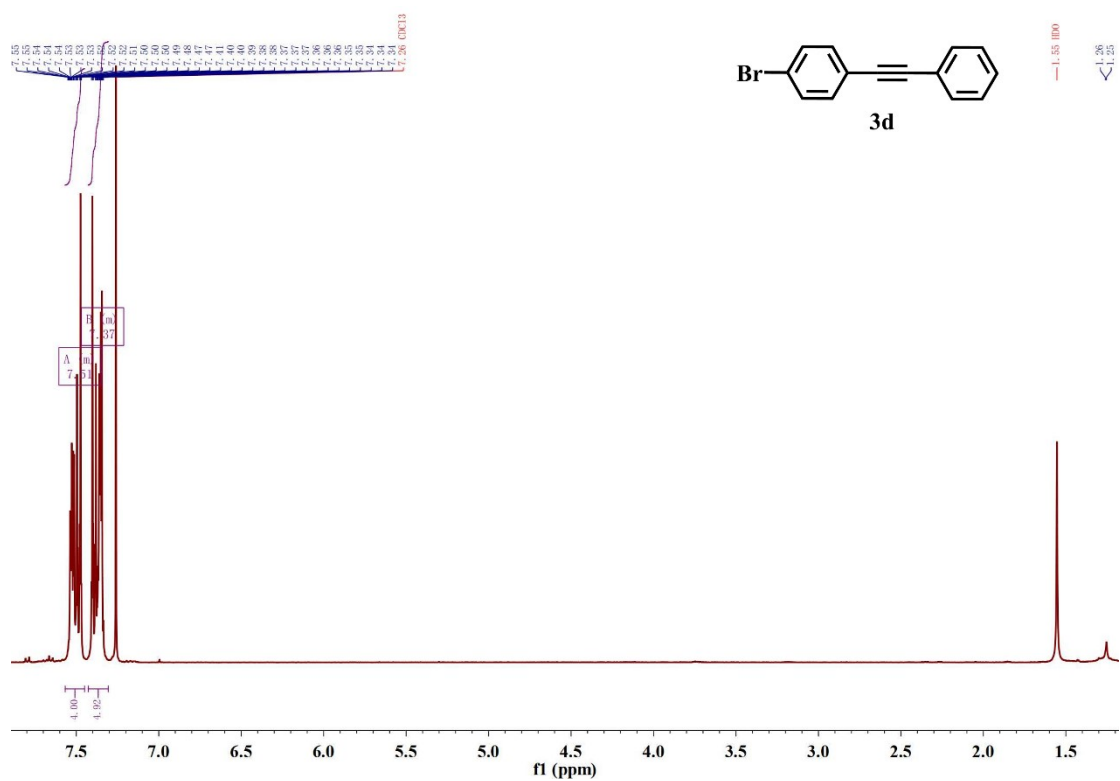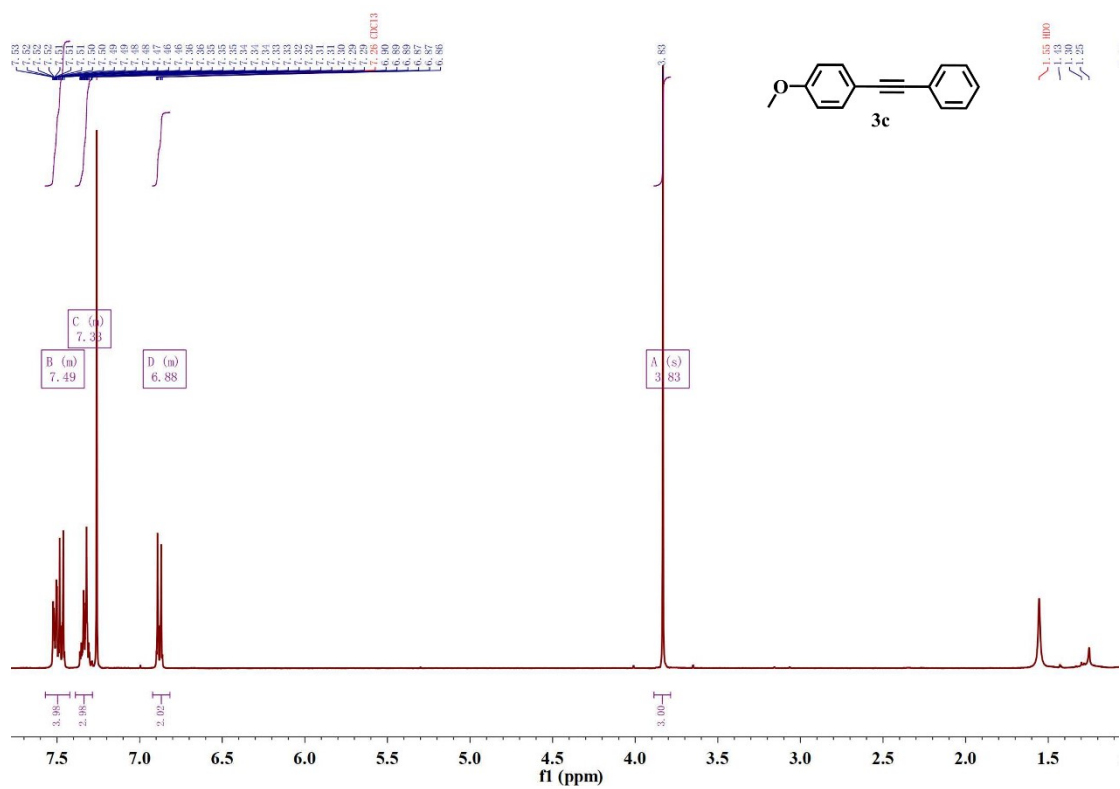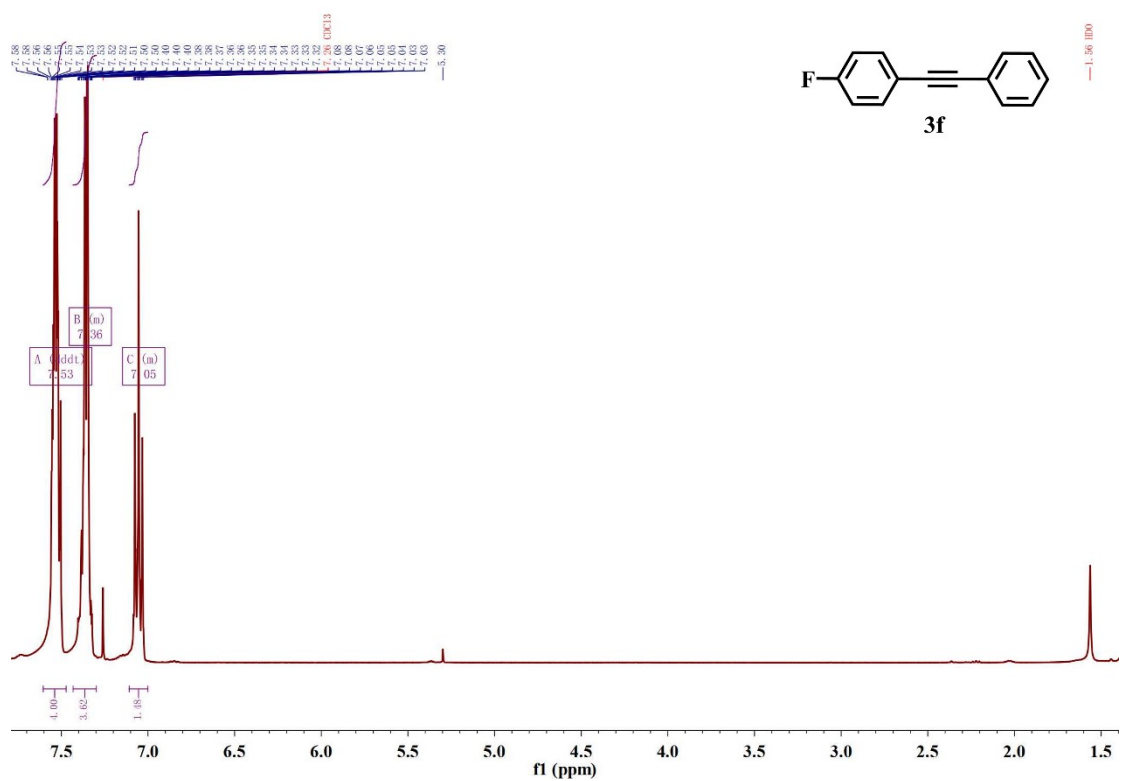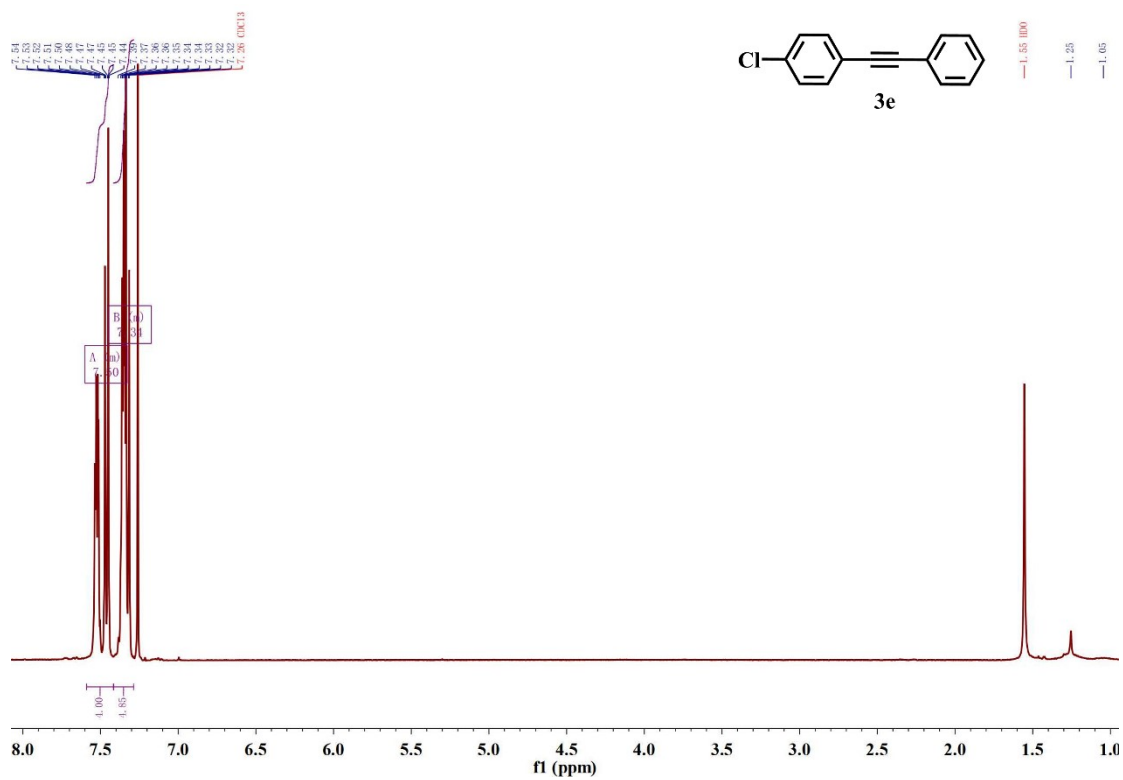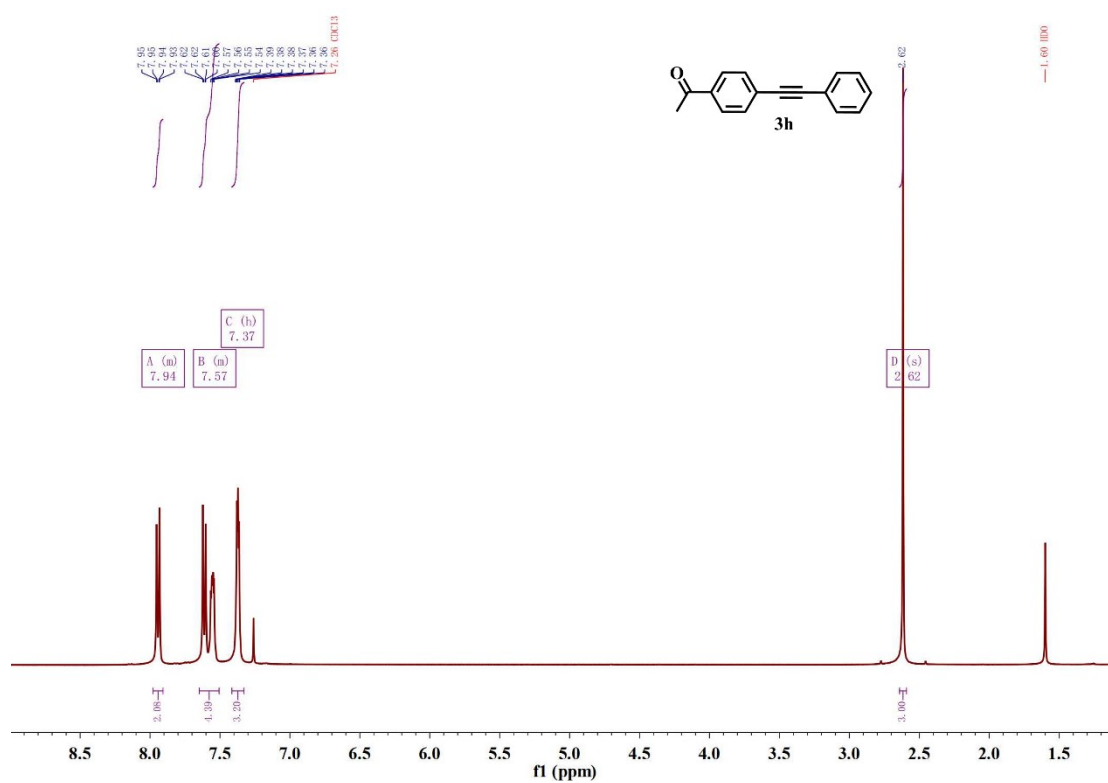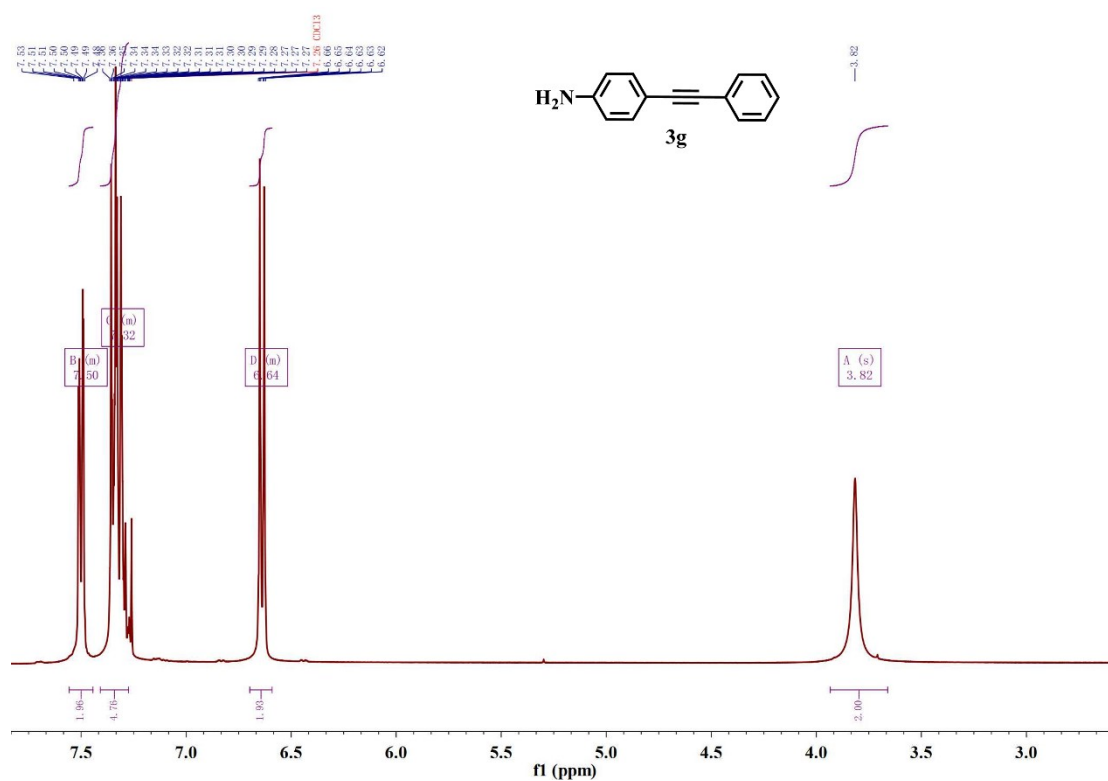
6.References

[1] M. Shunmughanathan, P. Puthiaraj and K. Pitchumani, *ChemCatChem,* 2015, **7**, 666-673.

[2] M. Shanmugam, A. Sagadevan, V. P. Charpe, V. K. K. Pampana and K. C. Hwan, *ChemSusChem,* 2010, **13**, 287.

[3] A.Sagadevan and K. C. Hwang, *Adv. Synth. Catal* ,2012, **354,** 3421-3427.

[4] M. H. Memon, U. E. S. Amjad, A. Mir and M. Mustafa, *ACS Appl. Electron. Mater.* 2024, **6**, 2178-2187.

[5] S. Potu, M. Navaneeth, A. Bhadoriya, A. Bora, Y. Sivalingam, A. Babu, M. Velpula, B. Gollapelli, R.K. Rajaboina, U.K. Khanapuram, H. Divi, P. Kodali and L. Bochu, *ACS Appl. Nano Mater.*, 2023, **6**, 22701-22710.

[6] Z. Chen, Y. Cao, W. Yang, L. An, H. Fan and Y. Guo, *J. Mater. Chem. A*, 2022, **10**, 799-807.

[7] R. A. Shaukat, S. Ameen, Q. M. Saqib, M. Y. Chougale, J. Kim, S. R. Patil, M. Noman, H. K. Kim and J. Bae, *J. Mater. Chem.* A, 2023, **11**, 14800-14808.

[8] S. Barsiwal, A. Babu, U.K. Khanapuram, S. Potu, N. Madathil, R.K. Rajaboina, S. Mishra, H. Divi, P. Kodali, R. Nagapuri and T. Chinthakuntla, *Nanoenergy Adv.*, 2022, **2**, 291-302.

[9] G. Khandelwal, N.P. Maria Joseph Raj and S.J. Kim, *Adv. Funct. Mater.*, 2020, **30**, 1910162.

[10] Abbas, M. Anithkumar, A. P. S. Prasanna, N. Hussain, Sang-Jae Kim and S. M. Mobin, *J. Mater. Chem. A*, 2023, **11**, 26531-26542.

[11] R.A. Shaukat, Q.M. Saqib, J. Kim, H. Song, M.U. Khan, M.Y. Chougale, J. Bae and M.J. Choi, *Nano Energy*, 2022, **96**, 107128.

[12] S. Barsiwal, A. Babu, U.K. Khanapuram, S. Potu, N. Madathil, R.K. Rajaboina, S. Mishra, H. Divi, P. Kodali, R. Nagapuri and T. Chinthakuntla, *Nanoenergy Adv.*,2022, **2**, 291-302.

[13] F. Wang, Y. Y. Zhang, S. Li, L. Zhang, Y. Tao, J. Cui and C. Huang, *Chem. Eng. J.*, 2025, **503**, 158194.